

Article

Petrogenesis and Geochronology of the Shazuoquan Ophiolite, Beishan Orogenic Belt: Constraints on the Evolution of the Beishan Ocean

Yong Meng^{1,2,*}, Xin Zhang^{1,2,*}, Jianke Bai^{1,2}, Kai Wang², Yaogang Qi¹, Haibo Zhao¹ and Yuan Han^{1,2}

¹ Xining Center of Natural Resource Comprehensive Survey, China Geological Survey (CGS), Xining 810021, China; baijianke2003@163.com (J.B.); 13519738002@163.com (Y.Q.); tiger_zhaohb@163.com (H.Z.); hyuan@mail.cgs.gov.cn (Y.H.)

² Xi'an Center of Geological Survey, China Geological Survey (CGS), Xi'an 710054, China; geo_wk@163.com

* Correspondence: myong@mail.cgs.gov.cn (Y.M.); gallery_zx@163.com (X.Z.)

Abstract: The ophiolites in the Beishan Orogenic Belt provide important information about the evolution of the Beishan Ocean in the Paleozoic Era. We studied ophiolite petrology, geochemistry and isotopic chronology. The Shazuoquan ophiolites consist of dunites, wehrlites, gabbros and anorthosites. Ophiolitic mélange belts are composed of matrixes and blocks, and different rocks are fault-bounded. Dunites and wehrlites are high in Mg[#], Cr[#] and MgO, low in TiO₂, relatively depleted in large-ion lithophile elements (Ti and P) and enriched in high-strength elements (U, Zr and Hf). They have a total REE of 1.25×10^{-6} – 5.39×10^{-6} and δEu of 1.12–3.54, which are similar to those of SSZ-type ophiolites, indicating that their parent magma source region may be a weakly depleted mantle source region. The anorthosite and gabbro are high in Al₂O₃, MgO and Mg[#], low in TiO₂, enriched in large-ion lithophile elements (Rb and Sr), and depleted in high-strength elements (Nb, Ta and Ti), but enriched in Zr and Hf. They have similar geochemical signatures to those of arc magmatic rocks. They are derived from the mantle peridotite formed against the tectonic background of subduction and modified by the fluid materials in the subduction zone. We collected anorthosite and gabbro, which were produced as ophiolite for U-Pb dating. The anorthosite yields a zircon U-Pb, aged 394 ± 11 Ma (MSWD = 0.84), and a gabbro zircon U-Pb, aged 466 ± 12 Ma (MSWD = 3.2), indicating that the Shazuoquan ophiolite was formed in the Middle Ordovician–Early Devonian eras. Combining the above evidence, we conclude that the Beishan Ocean was in a subduction tectonic background from the Middle Ordovician to Early Devonian periods.

Keywords: ophiolite; geochemistry; tectonic settings; Beishan Ocean; Shazuoquan



Citation: Meng, Y.; Zhang, X.; Bai, J.; Wang, K.; Qi, Y.; Zhao, H.; Han, Y. Petrogenesis and Geochronology of the Shazuoquan Ophiolite, Beishan Orogenic Belt: Constraints on the Evolution of the Beishan Ocean. *Minerals* **2023**, *13*, 1067. <https://doi.org/10.3390/min13081067>

Academic Editor: Rubén Díez-Fernández

Received: 17 June 2023

Revised: 5 August 2023

Accepted: 7 August 2023

Published: 11 August 2023



Copyright: © 2023 by the authors. Licensee MDPI, Basel, Switzerland. This article is an open access article distributed under the terms and conditions of the Creative Commons Attribution (CC BY) license (<https://creativecommons.org/licenses/by/4.0/>).

1. Introduction

The Beishan Orogenic Belt (BOB) is located on the southern margin of the Central Asian Orogenic Belt (CAOB) (Figure 1a) and has undergone complex processes of subduction, collision and accretion orogeny [1–17]. Several ophiolite belts in the BOB provide important geological records of the formation and evolution of the BOB, and are of great significance for the study of the formation and evolution of the BOB and the Paleo-Asian Ocean (PAO) [18–22]. Four different ophiolites have been identified in the BOB and they include the Hongshishan–Baiheshan–Pengboshan (I), Jijitaizi–Xiaohuangshan (II), Hongliuhe–Niujuanzi–Xichangjing (III), and Huitongshan–Zhangfangshan (IV) (Figure 1b). Among them, the Hongliuhe–Niujuanzi–Xichangjing ophiolite and the Jijitaizi–Xiaohuangshan ophiolite were formed in the Early Paleozoic era [23–28], and the Hongshishan–Baiheshan–Pengboshan ophiolite and the Huitongshan–Zhangfangshan ophiolite were formed in the Late Paleozoic era [29–33]. Therefore, the Hongliuhe–Niujuanzi–Xichangjing ophiolite belt constitutes a complex suture zone between the Tarim Block and the Kazakhstan United

Block. However, scholars differ in their understanding of the age of formation and tectonic setting of the Huitongshan–Zhangfangshan ophiolite. Li et al. [34] propose an Early Paleozoic island arc tectonic setting. In contrast, Mao et al. [35] favor a Carboniferous–Permian forearc tectonic setting. Conversely, Zhang et al. [25] suggest a Late Paleozoic post-collisional rift tectonic setting. Yu et al. [36] suggest that the Huitongshan ophiolite and the Zhangfangshan ophiolite may not be the same ophiolite belt, with formation ages of 446.1 ± 3 Ma and 362.6 ± 4 Ma, respectively. They conclude that the Huitongshan ophiolite formed in an ocean basin margin rift environment, while the Zhangfangshan ophiolite formed in a Late Paleozoic Red-Sea-type ocean basin environment.

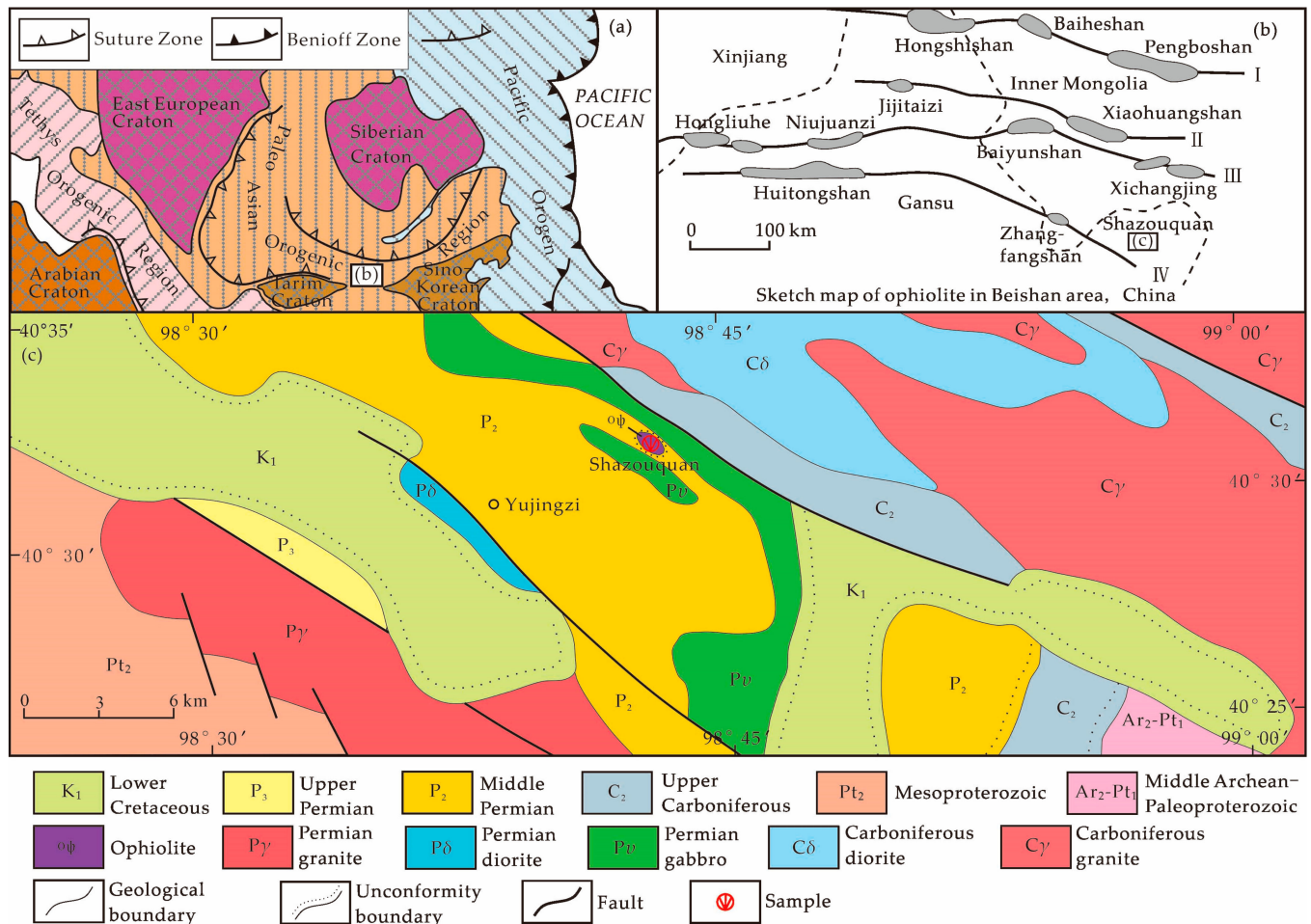


Figure 1. Simplified tectonic map showing the location of the Central Asia orogenic belt [10] (a); sketch map showing the tectonic units of the Beishan orogenic belt [21] (b); simplified geological map of the regions in Shazouquan [37] (c).

The Shazouquan Ophiolite Belt is located about 130 km east of the Zhangfangshan Ophiolite Belt. It lies on the same tectonic line as the Huitongshan Ophiolite Belt and the Zhangfangshan Ophiolite Belt, which extend in an almost east–west direction. Identifying the relationship between the Shazouquan Ophiolite Belt, the Huitongshan Ophiolite Belt and the Zhangfangshan Ophiolite Belt is of great importance in studying the tectonic pattern and evolutionary history of the BOB. During field investigations, we collected a series of samples for use in further systematic petrological, geochemical, and isotopic chronological studies on the peridotite, diorite and gabbro–diabase of the ophiolite. These studies provided a basis for the further investigation of the Paleozoic tectonic evolution of the BOB and CAO.

2. Geological Setting

The BOB is bounded by the South Mongolian Orogenic Belt to the north, the Tianshan Orogenic Belt to the west, the Dunhuang Block to the south and the Badanjilin Desert to the east. Archaean to Mesozoic strata are exposed in the Beishan area (Figure 1c). Archaean to Paleoproterozoic strata are mainly a series of metamorphic rocks [38]. The Mesoproterozoic to Cambrian strata are mainly a series of sedimentary formations, and the Ordovician–Permian strata are mainly volcanic–sedimentary formations [39]. The intrusive rocks in the Beishan area can be divided into four stages of magmatic intrusion: Precambrian, Early Paleozoic–Middle/Late Paleozoic ocean–land evolutionary stage, Mid–Late Paleozoic post-orogenic extension and continental rift valley stage, and Late Paleozoic–Mesozoic intra-continental evolutionary stage. The intrusive with the largest exposed area is the Late Paleozoic intrusive. The BOB is characterised as a thrust fold zone with multi-phase complex tectonic superposition. The Shazouquan Ophiolite is located in the Shazouquan area in the northern part of Jinta County, Gansu Province, and is linear in shape. Some 2 km long and only 100 m wide, the Shazouquan Ophiolite is surrounded by the Permian Jinta Formation and intruded by Permian gabbro veins. The Jinta Formation is a sequence of volcanic–sedimentary rock systems, consisting mainly of medium-acid and acid–basic volcanic rocks. There is no direct contact between the Shazouquan Ophiolite and the Jinta Formation due to the influence of overburden, which is speculated to be a form of tectonic contact. The ophiolitic mélangé belt is composed of matrix and blocks, and different rocks are fault-bounded. The ophiolite rocks include brown–green medium–fine dunite, grey–black medium–fine peridotite, grey fine-grained gabbro and grey medium–fine plagioclase (Figure 2), and different blocks of rocks are in fault contact.

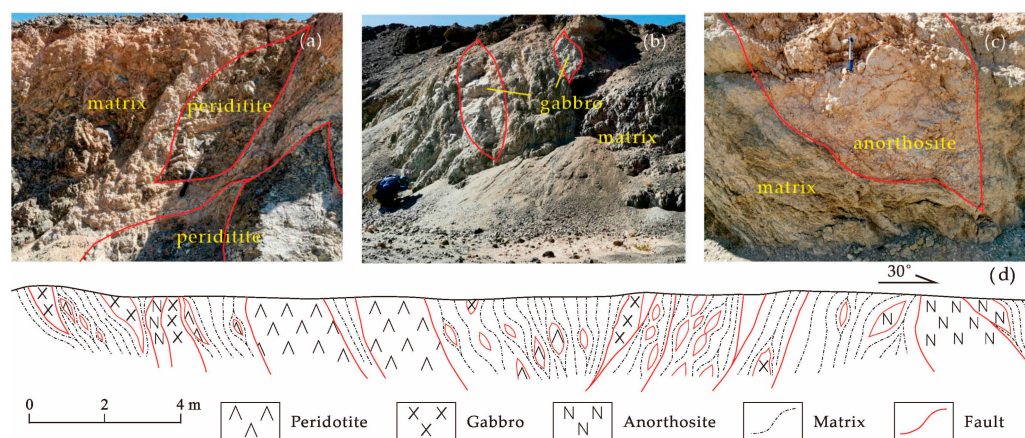


Figure 2. Cross-section of the ophiolitic tectonic mélangé belt in the BOB (d). (a) Peridotite; (b) Gabbro; (c) Anorthosite.

3. Petrography

Dunite appears greyish–brown with medium-grained crystals that range from subhedral to euhedral. It has the main minerals of olivine (91%), serpentine (7%), and pyroxene (2%), as well as opaque minerals (4%). The olivine is subhedral to euhedral crystals, is 0.42–4.2 mm in size, and sees small amounts altered into serpentine via magnetite precipitation. Pyroxene arrives in the form of subhedral crystals. They are short, columnar and granular, 0.06–0.74 mm in size, and mainly fine-grained (Figure 3a).

The wehrlite appears greyish–black, with medium- to fine-grained crystals that are euhedral. The main minerals are olivine (85–90%), serpentine (5–10%), clinopyroxene (2–5%) and tremolite (0–1%). Olivine is expressed in subhedral to euhedral crystals, which are 0.26–4.1 mm in size. Some samples are secondarily turned into sheet chrysotile and residual subhedral–euhedral crystals, and local alteration is completed to form a pseudostructure with residual euhedral crystals. This process involves partly cutting through the lattice using serpentine, with magnetite precipitation visible at the margins. Clinopyroxene is

expressed in euhedral crystals, short columnar or grains that are 0.06–1.1 mm in size, with some secondary alterations into fibrous serpentine. Some samples show opaque minerals, mainly magnetite. (Figure 3b).

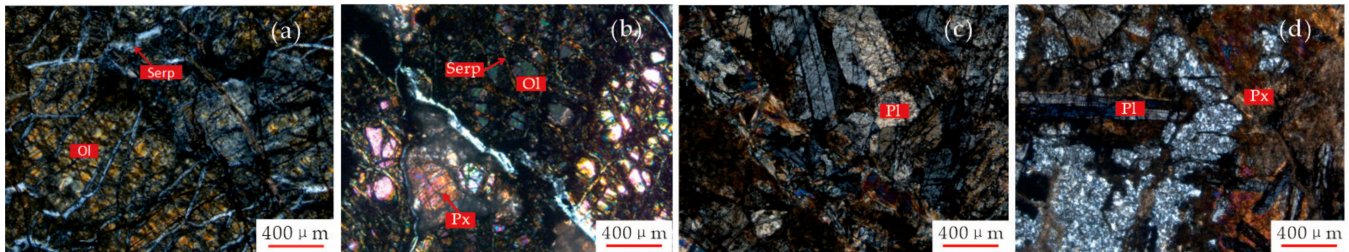


Figure 3. Microscopic images of the ophiolitic mélangé. (a) Dunite orthogonal photomicrograph. (b) Wehrlite orthogonal photomicrograph. (c) Anorthosite orthogonal photomicrograph. (d) Gabbro orthogonal photomicrograph. Ol = olivine; Serp = serpentine; Px = pyroxene; Pl = plagioclase.

The anorthosite appears to be light grey, with medium-to-fine-grained crystals that are euhedral. The main minerals are plagioclase (90%), carbonate minerals (7%), clinopyroxene (2%), and small amounts of zoisite and magnetite. The plagioclase is made of subhedral crystals, which are 0.06–4.1 mm in size, and developed with polycrystalline doublets, mainly labradorite. Carbonate minerals mainly occur as veinlets and alteration minerals. The clinopyroxene is made of grains that are 0.04–0.24 mm in size. The samples have a high content of alteration minerals with an uneven mineral distribution and show strong tectonic deformation characteristics, with some alteration minerals distributed along the veins, which are dominated by carbonation, silicification, zoisite, etc. (Figure 3c).

The gabbro appears to be greyish–green, with medium-to-fine-grained gabbroic structure. The main minerals are plagioclase (55–65%) and pyroxene (35–45%). The plagioclase is composed of subhedral crystals, which are 0.06–2.35 mm in size, mainly oligoclase. The pyroxene is composed of subhedral columnar crystals, which are 0.2–2 mm in size, mainly clinopyroxene. There are veinlets of carbonate veins and chlorite with local silicification in the samples, which are all characteristics of a secondary alteration (Figure 3d).

4. Isotope Chronology

In this study, anorthosite and gabbro samples were collected from Shazouquan Ophiolite for zircon U–Pb dating. Samples were crushed to a mesh size of 80–100 and separated via conventional heavy liquid and electromagnetic separation after cleaning. Zircons were selected by hand under a binocular microscope. Those with a good crystal shape and high transparency without inclusions or cracks were selected for analysis. The selected zircons were embedded in epoxy resin and polished to expose their interior. Transmitted and reflected light microscopy and cathodoluminescence (CL) helped to reveal the internal structure of the zircons to help select the optimal site for laser ablation inductively coupled plasma mass spectrometry (LA-ICP-MS).

The zircon CL and laser ablation plasma mass spectrometry (LA-ICP-MS) zircon micro-area U–Pb dating was completed in the Test Center of Xi’an Geological Survey Center, China Geological Survey. The experiment was carried out online using Agilent 7500 ICP-MS, a ComPex 102 ArF excimer laser (working material ArF, wavelength 193 nm) from Lambda Physik, Germany, and a GeoLas 200M optical system from Micro Las. The laser beam spot diameter was 30 µm. The depth of the exfoliated sample was 20–40 µm. In the experiment, He was used as the carrier gas for the erosion material, and the instrument was optimized using the artificially synthesized silicate glass standard reference material NIST SRM 610 developed by the National Institute of Standards and Technology of the United States. The sampling method involved single point erosion, and the data collection adopted a skip peak method of one quality peak and one point. We added a standard sample (standard zircon 91500) for every 6 measurement points completed. The NIST

SRM 610 was measured twice before and after analysing 12 points of the measured zircon. The zircon age was determined using the standard zircon 91,500 as the external standard reference material, and the ordinary lead was corrected using Andersen's 3D coordinate method. The element content adopted NIST SRM 610 as the external standard and ^{29}Si as the internal standard. The test results were calculated using GLITER (ver 4.0) software [40], and the age calculation and harmonic plot were completed using Isoplot (ver 3.0) [41]. The detailed analysis steps and data-processing methods can be found in the references [42], and the analysis results can be found in Table S1.

The zircons of anorthosite and gabbro are mostly euhedral–subhedral equigranular, or short columnar, and the grain size is mostly 50–120 μm . The CL image (Figure 4) shows that the zircons often have complex internal structures. According to the differences in the internal structure of the zircons, they can be divided into four types: The first category is made of zircons with wide oscillatory zones, which are crystallized under high-temperature conditions, such as points 4, 6, 7, 11, and 19 in the anorthosite samples (BS01) and points 9, 11, and 13 in the gabbro samples (BS07). The second type is the formation of narrow oscillatory zones at the edges of the zircon, such as points 5, 8–10, 12, 18, and 20 in the BS01 sample and 1–5, 8, 10, 12–16, 19, 22, and 23 in the BS07 sample. The third type is zircon without obvious oscillatory zones, such as points 1–3, 13, 14, 22, and 23 of the BS01 sample and points 7, 17, 18, 20, and 21 of the BS07 sample. The fourth type is zircon with clear surface zones, such as point 15 of the BS01 sample and points 6 and 9 of the BS07 sample. As shown in Table S1, the Th/U ratios of the two samples range from 0.25 to 1.34, indicating that the zircon is predominantly magmatic zircon (the Th/U ratio of metamorphic zircon is generally <0.1) [43–45].

The youngest zircon ages in the anorthosite samples (BS01) are 282 ± 3.75 Ma and 280.1 ± 3.45 Ma (the same zircon). The zircon has no oscillatory zones and appears in a clear, cloud-like form [43–45]. In addition, a metamorphic event occurred in about 280 Ma in the Eastern Tianshan Orogenic Belt and the BOB, so we can speculate that this was a metamorphic age. A number of large-scale ductile shear zones, such as the northern margin of Central Tianshan-Beishan, the southern margin of Central Tianshan, the northern part of Kuruktag and Xingdi, and arc-related developed in the Tianshan–Beishan orogenic belt, with the Late Carboniferous–Early Permian (298–277 Ma) period being one of the main periods of activity [46]. The other recent group ranges from 382 to 403.5 Ma, and the zircons are euhedral–subhedral with clear oscillatory zones, indicating a magmatic origin [44,45]. The weighted mean age is 394 ± 11 Ma (MSWD = 0.84) (Figure 5a), representing the crystallization of the anorthosite. The remainders are all captured zircons with a wide range of ages from 503.9 to 2533.7 Ma; this is consistent with the fluid metasomatism characteristics of the subduction zone, as reflected in the geochemical characteristics of anorthosite. The youngest age of the gabbro sample (BS07) is 442.3–504.8 Ma, and the zircons are euhedral–subhedral with clear oscillatory zones, which are magmatic zircons. The weighted mean age is 466 ± 12 Ma (MSWD = 3.2) (Figure 5b), representing the crystallization of gabbro. The remainders are trapped zircons with ages ranging from 1686.8 to 2534.8 Ma; this is consistent with the fluid metasomatism characteristics of the subduction zone, as reflected in the geochemical characteristics of gabbro.

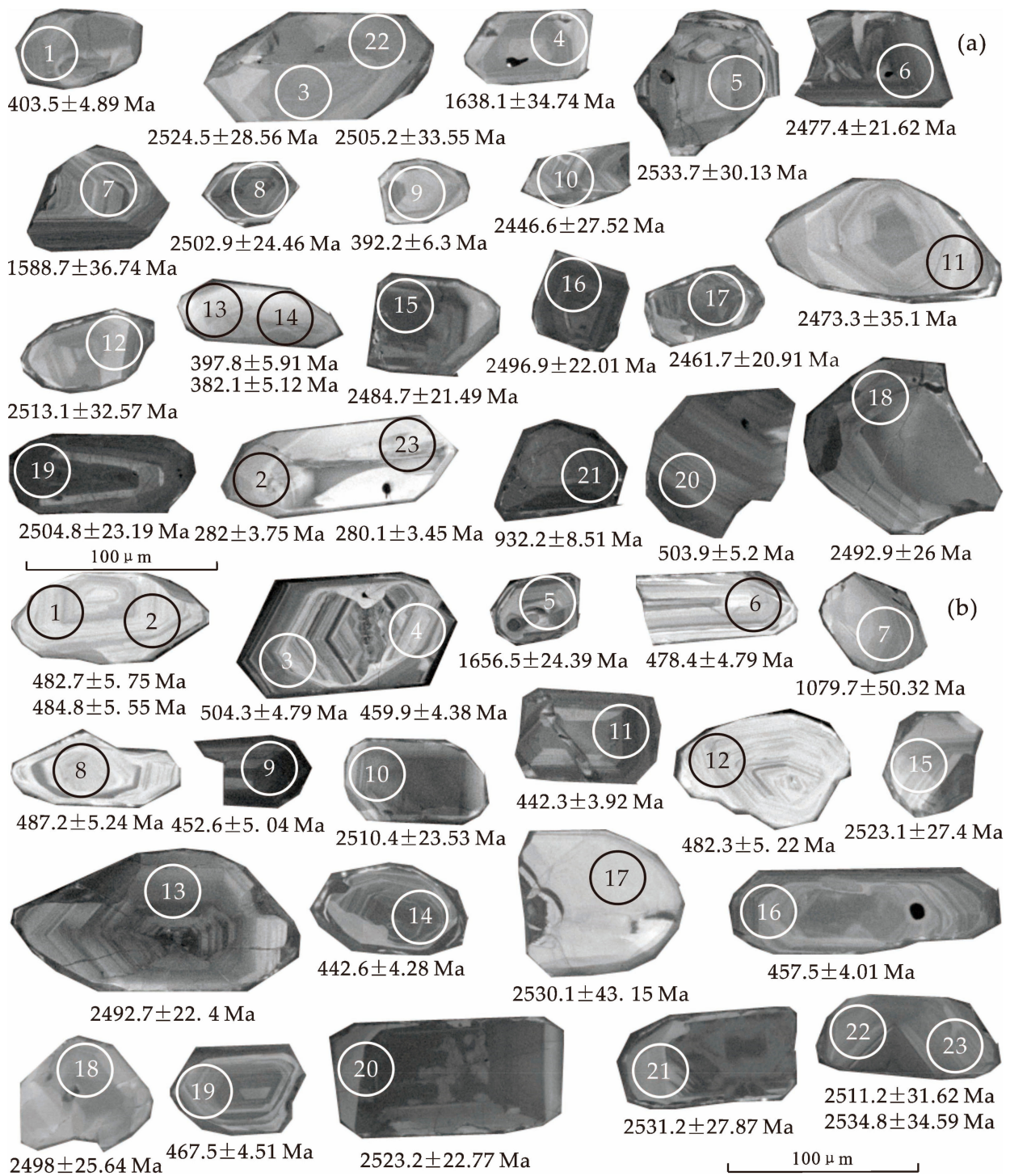


Figure 4. Zircon CL images of Shazouquan mafic rocks in the BOB. (a) CL images of anorthositic zircon (sample BS01). (b) CL images of gabbro zircon (sample BS07).

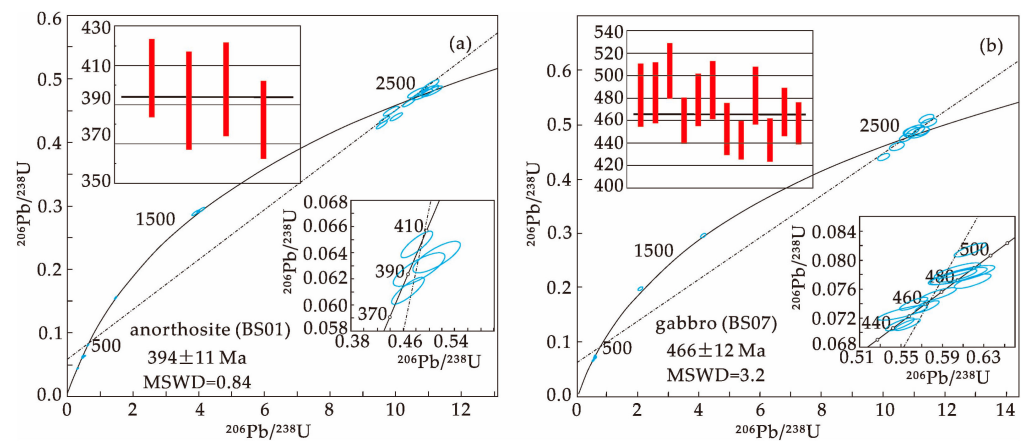


Figure 5. Concordance and weighted mean age plots (a,b) of LA-ICP-MS zircon U-Pb ages for Shazouquan mafic rocks in the BOB. (a) Anorthosite (BS01). (b) Gabbro (BS07).

5. Geochemistry

In this study, we collected twenty-nine fresh rock samples for geochemical analysis, including five dunite, twelve wehrlite, six anorthosite, and six gabbro ones. Elemental geochemical analysis was carried out in the Key Laboratory of Magmatism Mineralisation and Prospecting, Natural Resources Department, Xi'an Geological Survey Center, China Geological Survey. Major elements were determined using a PW4400 X-ray fluorescence spectrometer (XRF) from the Panalytical Company, and the analytical error was less than 5%; trace elements and rare earth elements were determined via ThermoFisher X-series II Inductively Coupled Plasma Mass Spectrometry (ICP-MS), and the relative standard deviation was better than 5%. The analytical data are presented in Table S2. The loss on ignition (LOI) values of ultramafic rock, anorthosite, and gabbro range from 9.55 wt.% to 12.38 wt.%, 4.51 wt.% to 7.91 wt.%, and 16.21 wt.% to 16.54 wt.%, respectively. This indicates that the rock samples underwent severe alterations, which is consistent with the thin section observations. The oxide content of the ultramafic rocks and anorthosite were recalculated after deducting the normalized loss on ignition, and the major elements of gabbro were not analysed (Table S2).

5.1. Ultramafic Rocks

The SiO₂ contents of the dunite and wehrlite samples range from 39.92 wt.% to 41.79 wt.%, and the MgO contents range from 36.41 wt.% to 42.37 wt.%. The Mg[#] values range from 84.17 to 86.51, and the TiO₂ contents range from 0.03 wt.% to 0.14 wt.%, with low amounts of titanium, potassium, and sodium, and a high amount of magnesium, which approximately represents the TiO₂ content of mantle peridites in the subduction zone [47]. Therefore, these ultramafic rocks may have been derived from the upper mantle beneath the subduction zone. In the CaO-MgO-Al₂O₃ diagram of the ophiolite (Figure 6), most of the samples fall within the mafic cumulate range, and individual samples fall between the ultramafic cumulate and metamorphic wehrlite, which is consistent with the petrographic characteristics.

The REE contents of dunite and wehrlite range from 1.25 to 5.39 ppm, with a very low total REE. Among them, five samples of dunite have ΣREE less than 2 ppm, which is lower than that of chondrite (3.29 ppm). The normalized REE distribution curve of the original mantle [48] shows the characteristics of a nearly flat "U" curve (Figure 7a), which is similar to the mantle peridotite of the SSZ-type ophiolite [49,50]. LREE/HREE = 1.95–5.36, and δEu = 1.12–3.54, and there are possible trace amounts of feldspar. The Cr contents range from 1350 to 2790 ppm, the Ni contents ranges from 879 to 1620 ppm, and Cr and Ni are highly enriched, which is similar to the geochemical composition of ultramafic rocks in typical ophiolites. The Cr and Ni contents are positively correlated with the MgO content (Figure 8), which contrasts with most of the Alpine ultramafic rocks in the world [51,52].

The standardized trace element discrimination diagram of the primitive mantle (Figure 7b) shows characteristic high left and low right curves. Sr, Rb, Ba, and other elements in sample 20BS04 are depleted, probably due to the migration of mobile elements via metamorphism, which is consistent with the petrographic characteristics.

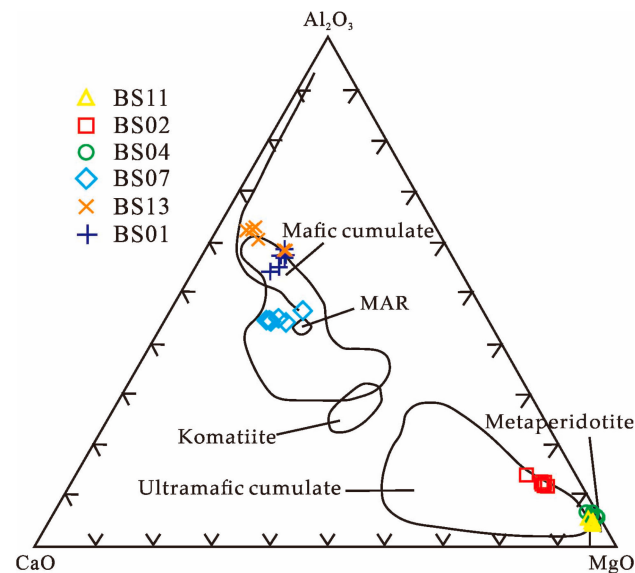


Figure 6. Plots of GaO-MgO-Al₂O₃ in Shazouquan ultramafic rocks in the BOB. MAR for average composition of oceanic ridge basalt [53].

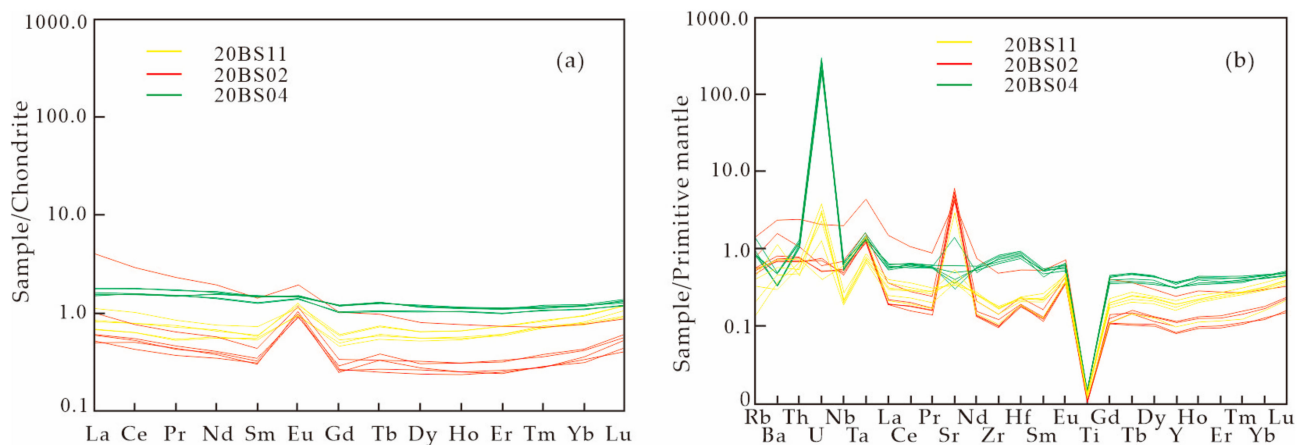


Figure 7. (a) Chondrite-normalized REE patterns. (b) Primitive mantle-normalized incompatible element distribution patterns for Shazouquan ultramafic rocks in the BOB (chondrite data and primitive mantle data for normalization taken from Sun et al. [54]).

5.2. Basic Rock

The anorthosite is characterised by low contents of SiO₂ (43.49 wt.%–45.42 wt.%) and TiO₂ (0.06 wt.%–0.14 wt.%), and the K₂O contents range from 0.11 wt.% to 0.38 wt.%, which is lower than the average values of oceanic ridge basalt and alkaline basalt (TiO₂ = 2.75 wt.%, K₂O = 3.2 wt.%). The Na₂O contents range from 2 wt.% to 3.07 wt.%, which is higher than the average content of MORB (0.14 wt.%). The Al₂O₃ contents range from 27.31 wt.% to 31.73 wt.%, the MgO contents from 36.41 wt.% to 42.37 wt.%, and the Mg[#] values range from 79.01 to 84.14, which are significantly higher than the initial magma Mg[#] values (68–75) [55]. The basement rocks are characterised by high Al₂O₃, MgO, and Mg[#] values and a low TiO₂ value. The samples are affected by late alterations; therefore, immobile

elements (Zr, Ti, Nb, Y, etc.) are used for rock type discrimination and genetic studies. In the Zr/TiO₂-Nb/Y diagram (Figure 10), 20BS13 falls into or near the subalkaline basalt zone, and 20BS01 falls into the calc-alkaline basalt series.

The REE contents of the basic rocks (gabbro and anorthosite) range from 3.43 to 11.92 ppm, which are much lower than the corresponding value of normal oceanic ridge basalt (39.11 ppm) [54], LREE/HREE = 1.85–2.65, δ Eu = 2.39–5.6, and the standardized curve of chondrites is right-leaning (Figure 9a), with an LREE that is slightly higher, but it flattens after Eu. The shape of the curve is significantly different from that of the N-MORB type, and the δ Eu positive anomaly is consistent with the characteristics of the cumulate (in Figure 7, anorthosite falls into the mafic cumulate range). The Zr/Hf ratio ranges from 23.36 to 42.3, which is close to that of the OIB (35.9) and primitive mantle (36.27) and much higher than that of the continental crust. The trace element spider discrimination diagram (Figure 9b) shows that gabbro and anorthosite have similar distributions and are obviously different from N-MORB. Overall, it is characterised by the enrichment of large ion lithophile elements, such as Rb and Sr, the depletion of high-field-strength elements, such as Nb, Ta, and Ti, and the depletion of Zr and Hf, which should be related to fluid metasomatism in the subduction zone at different levels in the later stage.

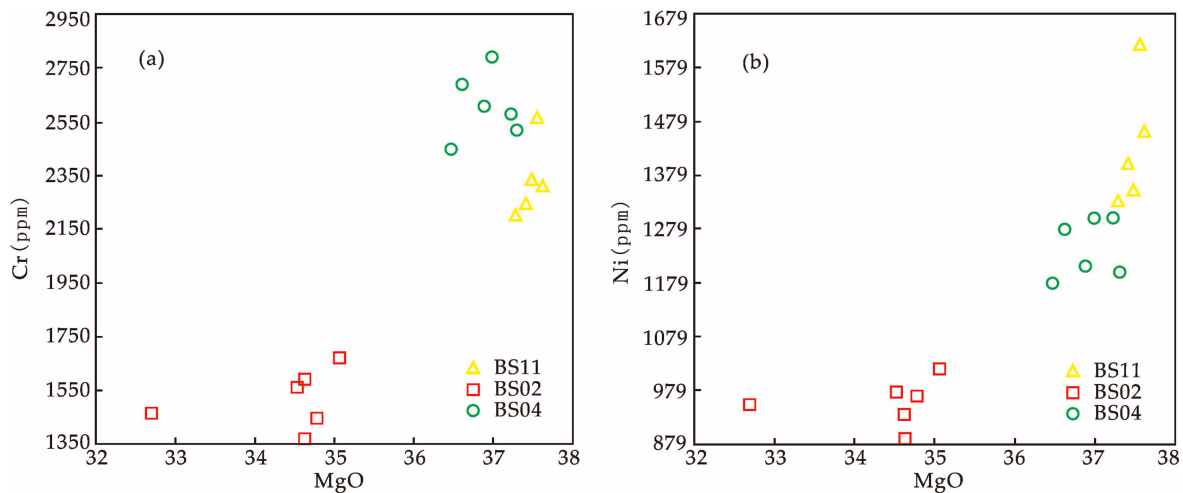


Figure 8. Covariation diagram of Cr (a) and Ni- (b) vs. MgO for Shazouquan ultramafic rocks in the BOB.

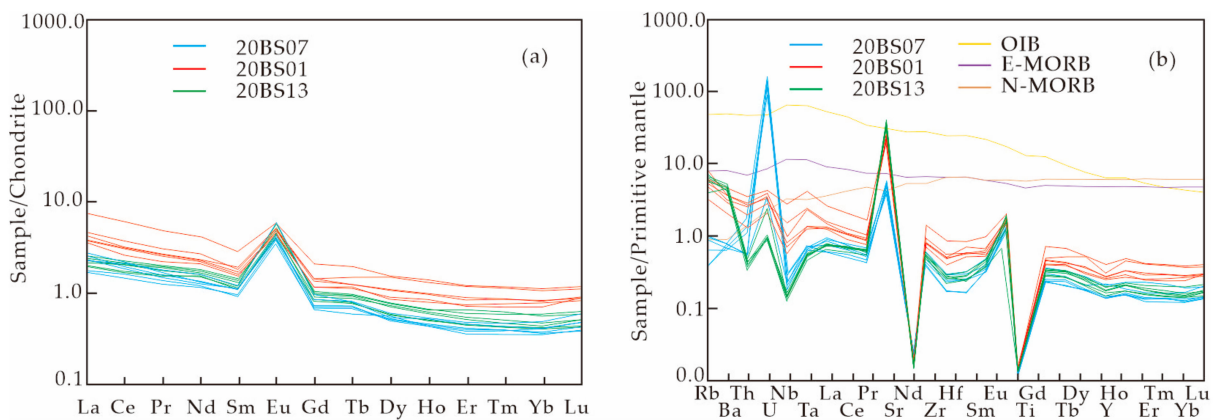


Figure 9. (a) Chondrite-normalized REE patterns. (b) Primitive mantle-normalized incompatible element distribution patterns for Shazouquan mafic rocks in the BOB (chondrite data and primitive mantle data for normalization taken from Sun et al. [54]).

6. Discussion

6.1. Petrogenesis

The geochemical characteristics of wehrlites and dunites in the Shazouquan Ophiolites show that these rocks are characterised by high $Mg^{\#}$ (84.17 to 86.51) $Cr^{\#}$ contents (48.79–83.52), a low TiO_2 content (0.03 wt.% to 0.14 wt.%), and a rich MgO content (36.41 wt.% to 42.37 wt.%), and their TiO_2 contents are roughly equivalent to those of mantle peridotites in the subduction zone [47], indicating that the ultramafic rocks may have originated from the upper mantle below the subduction zone and have strong residual characteristics of the depleted mantle. The relatively high $Mg^{\#}$ values also reflect the relatively high degree of mantle depletion and partial melting [48,56,57]. The MgO contents of the rocks are much higher than those of the original mantle, indicating that the olivine contents in dunites and wehrlites are much higher than those of the original mantle and have undergone a relatively high degree of mantle depletion or partial melting. In addition, the contents of major elements, such as SiO_2 , FeO^T , CaO, Al_2O_3 , and MnO, show a strong negative correlation with the contents of MgO, also reflecting the different degrees of partial melting of the rocks. On the primitive mantle-normalized trace-element spider diagram, the high-field-strength elements (HFSE, Zr, and Hf) are relatively enriched, and the large-ion lithophile elements (LILE, Ti, and P) are relatively depleted, suggesting that they may have originated from the weakly depleted mantle source area and are subject to different degrees of metasomatism from subduction fluids [58]. The significant enrichment of the U element also points to the role of crustal-derived fluids in the subduction zone. The characteristics of the primitive mantle-normalized REE distribution curve are similar to those of the mantle peridotites of the SSZ-type ophiolites, while the relative enrichment of LREEs may be modified by the subducted slab-derived fluid [59]. The significantly different REE abundances of wehrlites and dunites may reflect not only early mantle metasomatism, but on the influence of subducting oceanic crustal fluids on the rocks.

The Nb/Yb ratios of anorthosite in the Shazouquan Ophiolite range from 0.84 to 3.28 (with only two values of 5.43 and 7.17), which are similar to those of the gabbro (Nb/Yb = 1.59–2.2), indicating that they have a similar mantle source area. The Th/Ta ratios of anorthosite and gabbro range from 1.48 to 6.82, which are similar to those of SSZ-type ophiolite (Th/Ta = 3–5) [60]. The Zr/Nb ratios range from 5.7 to 31.3 (mean 16.5, except for one value > 30), which are significantly different from those of N-MORB [61]. The anorthosite and gabbro are also characterised by variable Th (0.02–0.17 ppm < 0.7 ppm) and Nb contents (0.09–1.97 ppm < 12 ppm), and Nb/La (0.19–1 < 1), Hf/Ta (1.5–4.5 < 5), and La/Ta values (10.4–29.5 < 15), which are different from those of N-MORB basalts [62]. The above characteristics are consistent with those shown in the REE distribution curve and trace-element spider diagram.

The anorthosite and gabbro are characterised by the enrichment of LILEs (e.g., Rb and Sr), the depletion of HFSE (e.g., Nb, Ta, and Ti), and a deficiency in Zr and Hf elements, which are also characteristics of arc magmas; these are consistent with the characteristics shown in the REE distribution curve and trace element spider diagram. The comprehensive analysis shows that gabbro and anorthosite are derived from mantle peridotite formed in the suprasubduction tectonic environment and have been altered by subduction zone fluids.

6.2. Tectonic Setting and Geological Significance

An ophiolite is a mafic–ultramafic rock assemblage that can be contrasted with the modern oceanic lithosphere and is widely used in the study of plate tectonic systems [50,52,63–66]. The classification scheme of mid-ocean ridge (MOR)-type ophiolites and subduction zone (SSZ)-type ophiolites proposed by Pearce et al. [50] is widely accepted. Dilek and Furnes [67] proposed a new definition of ophiolites, emphasizing the different nature of ophiolite formations at each stage of the Wilson cycle, and dividing ophiolites into subduction-unrelated and subduction-related ones according to their genesis environment. Based on the geochemical, petrographic and internal structural characteristics of ophiolites, the subduction-independent ophiolites can be further subdivided into continental

margin (CM), mid-ocean ridge (MOR) and mantle plume (P) ophiolites, and subduction-related ophiolites can be divided into supra-subduction zone (SSZ)-type and volcanic arc (VA)-type ones, while the SSZ type can be divided into four subtypes, including back-arc-to-fore-arc (BA-FA), fore-arc (FA), oceanic back-arc (OBA), and continental back-arc (CBA) ones. Among these, SSZ-type ophiolites are currently the most widespread ophiolite types [50,67,68].

The mantle peridotites in the MORB ophiolites are predominantly lherzolite and harzburgite [50], and the by-mineral spinel has a $Cr^{\#}$ value below 0.6 [52,69]. The mantle peridotite in the Shazouquan Ophiolite consists mainly of wehrlite and dunite, no lherzolite was found, and the rock is characterised by high $Mg^{\#}$ and $Cr^{\#}$ contents. The characteristics of the primitive mantle-normalized REE distribution curve are similar to those of the mantle peridotites of SSZ-type ophiolites. The trace element geochemistry of anorthosite and gabbro also shows the characteristics of SSZ-type ophiolites. In the Nb/Yb vs. Th/Yb and Nb/Yb vs. TiO_2/Yb discrimination diagrams (Figure 10), the sample points are relatively scattered, which is possibly related to the subduction oceanic crustal fluids. In the $Nb \times 2-Zr/4-Y$, $TiO_2.MnO \times 10-P_2O_5 \times 10$ and $Hf/3-Th-Nb/16$ diagrams (Figure 11), most of the samples are plotted in the island arc alkaline basalt region.

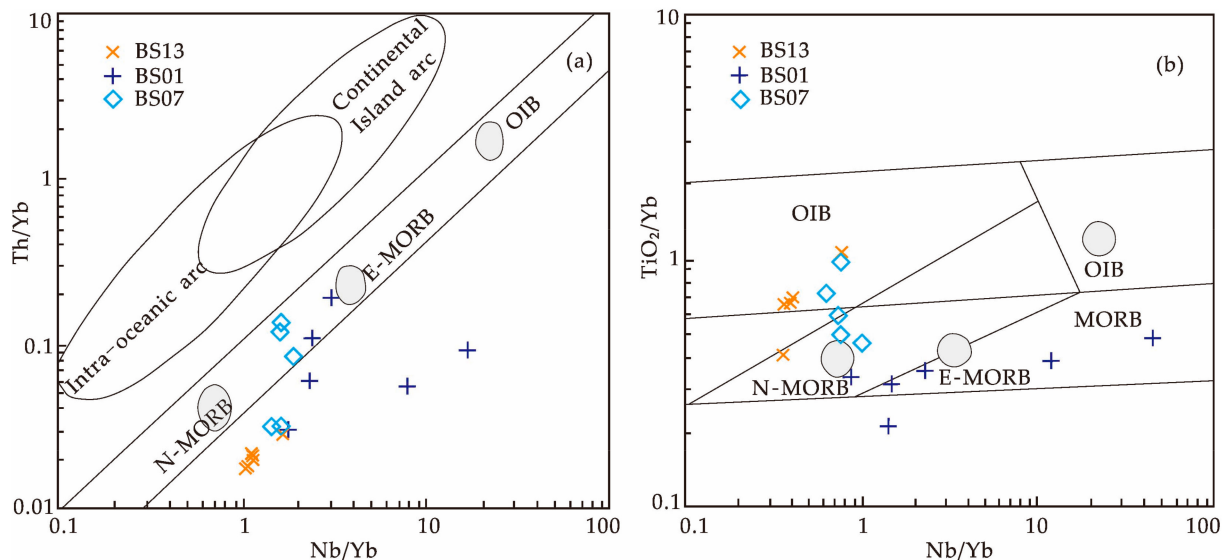


Figure 10. Plots of Nb/Yb-Th/Yb (a) and Nb/Yb-TiO₂/Yb (b) in Shazouquan mafic rocks in the BOB [54]. MORB stands for mid-ocean ridge basalts; N-MORB stands for normal MORB; E-MORB stands for enriched MORB; OIB stands for ocean island basalts.

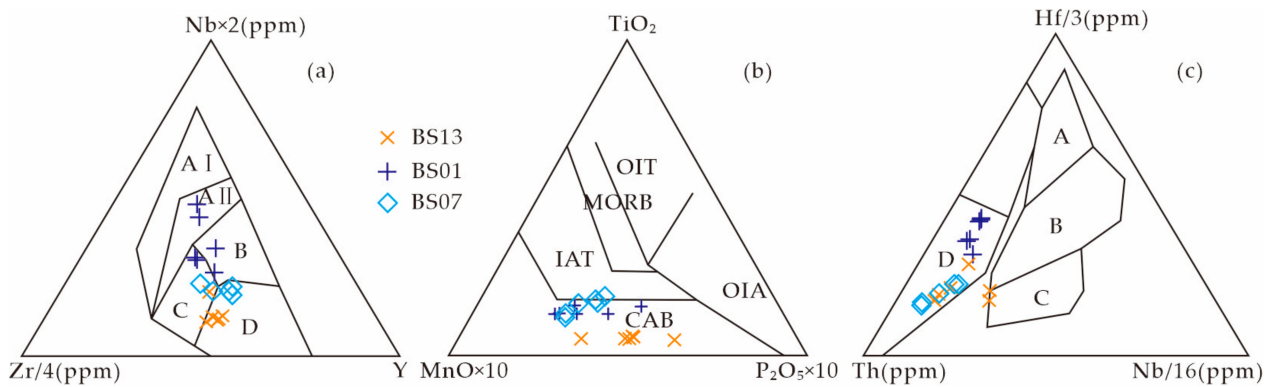


Figure 11. Plots of Shazouquan anorthosite and gabbro Nb × 2-Zr/4-Y (a) [70], TiO₂-MnO × 10-P₂O₅ × 10 (b) [71], and Hf/3-Th-Nb/16 (c) [72] in the BOB. Nb × 2-Zr/4-Y diagram: AI stands for within-plate alkaline basalts, AII stands for within-plate alkaline basalts and within-plate tholeiitic, B stands for E-MORB, C stands for within-plate tholeiitic and volcanic-arc basalts, and D stands for depleted MORB and volcanic-arc basalts. TiO₂-MnO × 10-P₂O₅ × 10 diagram: OIT stands for ocean island tholeiitic, MORB stands for mid-ocean ridge basalts, IAT stands for island-arc tholeiitic, OIA stands for ocean island alkaline, and CAB stands for calc-alkaline basalts. Hf/3-Th-Nb/16 diagram: A stands for depleted MORB, B stands for E-MORB and within-plate tholeiitic, C stands for within-plate tholeiitic, and D stands for volcanic-arc basalts.

The Hongliuhe–Niuquanzi–Xichangjing ophiolite mélangé belt is related to the South Tianshan Suture Zone, which is a suture zone between the Tarim block and the Kazakhstan block [3,11,23–28,73–79]. There are various views on the timing of the closure of the Southern Ocean, including the Late Devonian [73,74], Early Carboniferous [75–79], Early–Middle Carboniferous [80–82], Late Carboniferous [83–87], Late Carboniferous to Early Permian [88], and Late Permian to Middle Triassic [87,89,90]. In the Beishan area, the Late Devonian Dundunshan Formation, which contains intraplate basalt, unconformity overlies the molasse of the Middle Devonian Sangejing Formation (Figure 12), which is regarded as a sign of ocean–continent conversion in the process of the Beishan–Paleozoic ocean basin [91], while the Ordovician–Devonian period has a tectonic background composed of subduction–collision. Therefore, from the perspective of regional tectonic evolution, the formation of the Shazouquan Ophiolite should be related to the geotectonic setting of the island arc. Although there is no Ordovician–Devonian granite exposed around the study area, Ordovician and Devonian island arc volcanics are exposed in the western area of Huitongshan. The lithological combination is composed of diorite, quartz diorite, monzogranite, and syenogranite, which are island arc igneous rocks that are compatible ophiolite [11,92].

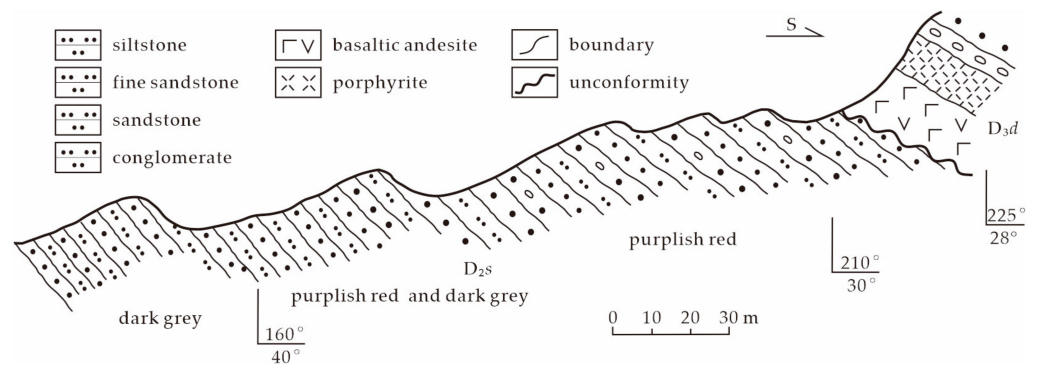


Figure 12. The geological section of Dundunshan formation and Sangejing formation in the BOB.

From the characteristics of the surrounding rocks, there is a Meso-archean-to-Paleoproterozoic Dunhuang Complex crystalline basement, Changchengian Gudongjing Group, and Meso-proterozoic Pingtoushan Formation metamorphic basement around the Shazouquan Ophiolite [11,93], which should belong to the subduction accretionary complex formed during the northward subduction of the Beishan Ocean, and its tectonic position is south of the Niuquanzi–Xichangjing main suture zone. Therefore, it should be a fore-arc ophiolite of the subduction zone hanging wall (SSZ) associated with subduction.

The Shazouquan Ophiolite is located to the east of the Huitongshan–Zhangfangshan ophiolite belt, with diagenetic ages of 466 ± 12 Ma and 394 ± 11 Ma, respectively. Anorthosite formed during the last stage of gabbro crystallization differentiation, and formed later than the ophiolite. The formation age of the Huitongshan ophiolite is between 466 ± 12 Ma and 394 ± 11 Ma, which means that it may belong to the same ophiolite tectonic mélange belt, and subduction lasted from the Middle Ordovician to the Early Devonian periods.

During ocean subduction, the fore-arc environment expands the oceanic floor, and the subduction plate is dehydrated, causing the mantle wedge to become hydrated. The weakly depleted mantle upwelling transfers heat to the overlying mantle wedge through the slab window, the temperature of the overlying mantle wedge rises, and partial melting occurs, and the mantle and overlying mantle wedge undergo magma mixing and contamination. Finally, Shazouquan ophiolite with SSZ ophiolite characteristics is formed in the fore-arc environment above the intra-oceanic subduction zone.

7. Conclusions

1. SSZ-type ophiolite is exposed in the Shazouquan area of the BOB. Shazouquan Ophiolites consist of dunites, wehrlites, gabbros, and anorthosites and have the typical characteristics of an ophiolitic mélange belt. The zircon U-Pb age of gabbro in the ophiolite is 466 ± 12 Ma (MSWD = 3.2), and the zircon U-Pb age of anorthosite is 394 ± 11 Ma (MSWD=0.84). The ophiolite was dated to a period from the Middle Ordovician to Early Devonian.
2. The wehrlite and dunite in the Shazouquan Ophiolite are characterised by high $Mg^\#$ and $Cr^\#$, low TiO_2 , and rich MgO contents, which may be derived from the weakly depleted mantle source area and due to varying degrees of metasomatism from subduction zone fluids.
3. The anorthosite and gabbro in the Shazouquan ophiolite are rich in Rb, Sr, and other LILEs, depleted in Nb, Ta, Ti, and other high field strength elements, and lacking in Zr and Hf elements. They are derived from the mantle peridotite formed under the tectonic background of subduction and have been modified by the fluid materials in the subduction zone.
4. Shazouquan Ophiolites may belong to the same ophiolitic mélange belt as Huitongshan ophiolites. The Beishan oceanic basin was located in a subduction tectonic setting during the Ordovician–Middle Devonian period, suggesting that the Beishan Ocean may have evolved as a trench arc basin system caused by plate subduction and subduction.

Supplementary Materials: The following supporting information can be downloaded from: <https://www.mdpi.com/article/10.3390/min13081067/s1>, Table S1: Zircon LA-ICP-MS U-Pb data of anorthosite and gabbro in the Shazouquan area, Beishan, China; Table S2: Major (wt.%) and trace (ppm) element concentrations of dunite, wehrlite, gabbro, anorthosite and plagiogranite in the Shazouquan area, Beishan, China.

Author Contributions: Conceptualization, Y.M. and X.Z.; methodology, Y.M. and X.Z.; software, J.B., H.Z. and Y.H.; validation, H.Z. and X.Z.; formal analysis, Y.M., X.Z., K.W., J.B. and Y.Q.; investigation, Y.M., X.Z., J.B., K.W., H.Z., Y.H. and Y.Q.; resources, Y.M. and X.Z.; data curation, Y.M. and X.Z.; writing—original draft preparation, Y.M. and X.Z.; writing—review and editing, Y.M., X.Z. and K.W.; visualization, Y.M.; supervision, Y.M. and X.Z.; project administration, Y.M. and X.Z.; funding acquisition, Y.M. and K.W. All authors have read and agreed to the published version of the manuscript.

Funding: This research was funded by the National Natural Science Foundation of China (Grant Nos. 42002229) and the China Geological Survey (Grant Nos. DD20190364, DD20220978).

Data Availability Statement: The original contributions presented in the study are included in the article/Supplementary Materials.

Acknowledgments: We are grateful to Rongshe Li of Xi'an Geological Survey Center of China Geological Survey, Xunlian Wang and Guocan Wang of China University of Geosciences, and Bei Xu of Hebei University of Geosciences for their guidance in the field work. We would like to thank Weiliang Li, Mengqi Jin, Xiaoyan Wei and others from the Experimental Testing Center of Xi'an Geological Survey Center of China Geological Survey for their help with sample analysis and testing. Special thanks are due to the reviewers and editors of this journal for their valuable suggestions and revisions of the manuscript.

Conflicts of Interest: The authors declare no conflict of interest.

References

1. Şengör, A.M.C.; Natal'in, B.A.; Burtman, V.S. Evolution of the Altaid tectonic collage and Paleozoic crustal growth in Eurasia. *Nature* **1993**, *364*, 299–307. [[CrossRef](#)]
2. Jahn, B.M.; Wu, F.Y.; Chen, B. Granitoids of the Central Asian Orogenic Belt and continental growth in the Phanerozoic. *Transactions of the Royal Society of Edinburgh. Earth Sci.* **2000**, *91*, 181–193.
3. He, S.P.; Ren, B.S.; Yao, W.G.; Fu, L.P. The division of tectonic units of Beishan area, Gansu-Inner Mongolia. *Northwest. Geol.* **2002**, *35*, 30–40. (In Chinese with English Abstract)
4. Gong, Q.S.; Liu, M.Q.; Li, H.L.; Liang, M.H.; Dai, W.J. The type and basic characteristics of Beishan orogenic belt, Gansu. *Northwest. Geol.* **2002**, *35*, 28–34. (In Chinese with English Abstract)
5. Zuo, G.C.; Liu, Y.K.; Liu, C.Y. Frame work and evolution of the tectonic structure in Beishan Area across Gansu Province, Xinjiang Autonomous Region and Inner Mongolia Autonomous Region. *Acta Geol. Gansu* **2003**, *12*, 1–15. (In Chinese with English Abstract)
6. Hong, D.; Zhang, J.; Wang, T.; Wang, S.; Xie, X. Continental crustal growth and the supercontinental cycle: Evidence from the Central Asian Orogenic Belt. *J. Asian Earth Sci.* **2004**, *23*, 799–813. [[CrossRef](#)]
7. Kovalenko, V.I.; Yarmolyuk, V.V.; Kovach, V.P.; Kotov, A.B.; Kozakov, I.K.; Salnikova, E.B.; Larin, A.M. Isotopic provinces, mechanism of generation and sources of the continental crust in the Central Asian mobile belt: Geological and isotopic evidence. *J. Asian Earth Sci.* **2004**, *23*, 605–627. [[CrossRef](#)]
8. He, S.P.; Zhou, H.W.; Ren, B.S.; Yao, W.G.; Fu, L.P. Crustal evolution of Paleozoic in Beishan area, Gansu and Inner Mongolia, China. *Northwest. Geol.* **2005**, *38*, 6–15. (In Chinese with English Abstract)
9. Kröner, A.; Windley, B.F.; Badarch, G.; Tomurtogoo, O.; Catalán, M. Accretionary growth and crust formation in the Central Asian Orogenic Belt and comparison with the Arabian—Nubian Shield. *Geol. Soc. Am. Mem.* **2007**, *200*, 181–209.
10. Windley, B.F.; Alexeiev, D.; Xiao, W.J.; Kröner, A.; Badarch, G. Tectonic models for accretion of the Central Asian Orogenic Belt. *J. Geol. Soc.* **2007**, *164*, 31–47. [[CrossRef](#)]
11. Xu, X.Y.; He, S.P.; Wang, H.L.; Chen, J.L.; Zhang, E.; Feng, Y.M. *Geology of Northwest China*; Science Press: Beijing, China, 2008; pp. 1–347. (In Chinese)
12. Xiao, W.J.; Mao, Q.G.; Windley, B.F.; Han, C.M.; Qu, J.F.; Zhang, J.E.; Ao, S.J.; Guo, Q.Q.; Cleven, N.R.; Lin, S.F.; et al. Paleozoic multiple accretionary and collisional processes of the Beishan orogenic collage. *Am. J. Sci.* **2010**, *310*, 1553–1594. [[CrossRef](#)]
13. Song, D.F.; Xiao, W.J.; Han, C.M.; Tian, Z.H. A Paleozoic Japan-type subduction-accretion system in the Beishan orogenic collage, southern Central Asian Orogenic Belt. *Lithos* **2015**, *224*, 195–213. [[CrossRef](#)]
14. Zong, K.Q.; Klemd, R.; Yuan, Y.; He, Z.Y.; Guo, J.L.; Shi, X.L.; Liu, Y.S.; Hu, Z.C.; Zhang, Z.M. The assembly of Rodinia: The correlation of early Neoproterozoic (ca. 900 Ma) high-Grade metamorphism and continental arc formation in the southern Beishan Orogen, southern Central Asian Orogenic Belt (CAOB). *Precambrian Res.* **2017**, *290*, 32–48. [[CrossRef](#)]
15. Shi, Y.R.; Zhang, W.; Krner, A.; Li, L.L.; Jian, P. Cambrian ophiolite complexes in the Beishan area, China, southern margin of the Central Asian Orogenic Belt. *J. Asian Earth Sci.* **2018**, *153*, 193–205. [[CrossRef](#)]
16. Wang, B.R.; Yang, X.S.; Li, S.C.; Teng, C.; Yang, X.J.; Huang, F.Y.; Zhang, X.F.; Cao, J.; Zhou, Y.; Zhang, H.C.; et al. Geochronology, geochemistry, and tectonic implications of early Neoproterozoic granitic rocks from the eastern Beishan Orogenic Belt, southern Central Asian Orogenic Belt. *Precambrian Res.* **2021**, *352*, 106016–106028. [[CrossRef](#)]
17. De Jordy, V.; Lin, S.F.; Cees Van, S.; Chris, Y. A structural–metamorphic study of the Gubaoquan eclogites and enveloping rock units in the Beishan Orogenic Collage, NW China, with emphasis on the structural evolution, nature of juxtaposition and exhumation. *Int. J. Earth Sci.* **2022**, *111*, 2603–2632.
18. Yu, F.S.; Wang, C.Y.; Qi, J.F.; Wang, T. The clarification and tectonic implication of the Early Silurian ophiolite mélange in Hongliuhe area. *J. Mineral. Petrol.* **2000**, *20*, 60–66. (In Chinese with English Abstract)
19. Wei, Z.J.; Huang, Z.B.; Jin, X.; Sun, Y.J.; Huo, J.C. Geological characteristics of ophiolite migmatitic complex of Hongshishan region, Gansu. *Northwest. Geol.* **2004**, *37*, 13–18. (In Chinese with English Abstract)

20. Huang, Z.B.; Jin, X. Tectonic environment of basic volcanic rocks in the Hongshishan ophiolite mélange zone, Beishan Mountains, Gansu. *Geol. China* **2006**, *33*, 1030–1037. (In Chinese with English Abstract)
21. Yang, H.Q.; Li, Y.; Zhao, G.B.; Li, W.Y.; Wang, X.H.; Jiang, H.B.; Tan, W.J.; Sun, N.Y. Character and structural attribute of the Beishan Ophiolite. *Northwest. Geol.* **2010**, *43*, 26–36. (In Chinese with English Abstract)
22. Wang, S.J.; Dai, P.; Wang, J.X.; She, Y.M.; Zhang, K.X.; Hu, Q.H. Mazongshan ophiolite in the Beishan Orogen, NW China: Relicts of the major branch of Paleo-Asian oceanic crust. *Int. J. Earth Sci.* **2022**, *111*, 2353–2367. [[CrossRef](#)]
23. Zhang, Q.; Zhou, G.Q.; Wang, Y. The distribution of time and space of Chinese ophiolites, and their tectonic settings. *Acta Petrol. Sin.* **2003**, *19*, 1–8. (In Chinese with English Abstract)
24. Dai, W.J. The formation background and tectonic significance of the ophiolite mélange in the Niuquanzi area, Beishan, Gansu Province. *J. Mineral Petrol.* **2011**, *31*, 44–51. (In Chinese with English Abstract)
25. Zhang, Y.Y.; Dostal, J.; Zhao, Z.H.; Chang, L.; Guo, Z.J. Geochronology, geochemistry and petrogenesis of mafic and ultramafic rocks from Southern Beishan area, NW China: Implications for crust–Mantle interaction. *Gondwana Res.* **2011**, *20*, 816–830. [[CrossRef](#)]
26. Wu, P.; Wang, G.Q.; Li, X.M.; Yu, J.Y.; Kang, L. The age of Niuquanzi ophiolite in Beishan area of Gansu Province and its geological significances. *Geol. Bull. China* **2012**, *31*, 2032–2037. (In Chinese with English Abstract)
27. Tian, Z.H.; Xiao, W.J.; Windley, B.F.; Lin, L.N.; Han, C.M.; Zhang, J.E.; Wan, B.; Ao, S.J.; Song, D.F.; Feng, J.Y. Structure, age, and tectonic development of the Huoshishan–Niuquanzi ophiolitic mélange, Beishan, southernmost Altai. *Precambrian Res.* **2014**, *25*, 820–841. [[CrossRef](#)]
28. Cleven, N.R.; Lin, S.F.; Xiao, W.J. The Hongliuhe fold-and-thrust belt: Evidence of terminal collision and suture-reactivation after the Early Permian in the Beishan orogenic collage, Northwest China. *Precambrian Res.* **2015**, *27*, 796–810. [[CrossRef](#)]
29. Li, X.M.; Yu, J.Y.; Wang, G.Q.; Wu, P. Geochronology of Jijitaizi ophiolite in Beishan area, Gansu Province, and its geological significance. *Geol. Bull. China* **2012**, *31*, 2025–2031. (In Chinese with English Abstract)
30. Wang, X.H.; Yang, J.G.; Xie, X.; Wang, L. The genetic type and tectonic significance of Hongshishan basic-ulteabasic Rocks in Beishan, Gansu Province. *Northwest. Geol.* **2013**, *46*, 40–55. (In Chinese with English Abstract)
31. Wang, G.Q.; Li, X.M.; Xu, X.Y.; Yu, J.Y.; Wu, P. Zircon U-Pb chronological study of the Hongshishan ophiolite in the Beishan area and their tectonic significance. *Acta Petrol. Sin.* **2014**, *30*, 1685–1694. (In Chinese with English Abstract)
32. Niu, W.C.; Ren, B.F.; Ren, Y.W.; Sun, L.X.; Duan, X.L.; Duan, L.F.; Li, M.; Zhang, J.H. Discovery of Neoproterozoic gneissic granite from the Beishan area, Inner Mongolia: Zircon U-Pb chronologic evidence. *Geol. China* **2017**, *44*, 409–410. (In Chinese with English Abstract)
33. Niu, W.C.; Xin, H.T.; Duan, L.F.; Wang, G.H.; Zhao, Z.L.; Zhang, G.Z.; Zheng, Y.L. The identification and subduction polarity of the Baiheshan ophiolite mélanges belt in the Beishan area, Inner Mongolia—New understanding based on the geological map of Qinghegou Sheet (1:50000). *Geol. China* **2019**, *46*, 977–994. (In Chinese with English Abstract)
34. Li, C.Y. China and its adjacent northern areas of the ancient border of plate tectonics and the formation of the Eurasian continent. *Collect. Work. Plate Tecton. North China* **1987**, 3–17. (In Chinese)
35. Mao, Q.G.; Xiao, W.J.; Windley, B.F.; Han, C.M.; Qu, J.F.; Zhang, J.E.; Guo, Q.Q. The Liuyuan complex in the Beishan, NW China: A Carboniferous–Permian ophiolitic fore–Arc sliver in the southern Altai. *Geol. Mag.* **2011**, *149*, 483–506. [[CrossRef](#)]
36. Yu, J.Y.; Li, X.M.; Wang, G.Q.; Wu, P.; Yan, Q.J. Zircon U-Pb ages of Huitongshan and Zhangfangshan ophiolite in Beishan of Gansu–Inner Mongolia border area and their significance. *Geol. Bull. China* **2012**, *31*, 2038–2045. (In Chinese with English Abstract)
37. Meng, Y.; Chen, F.N.; Yu, J.Y.; Ji, W.H.; Feng, Y.M.; Zhang, X.; Gu, P.Y.; Li, X.M.; Wang, K.; Zhu, X.H.; et al. *Tectonic Evolution in Northwest China and its Adjacent Areas*; China University of Geosciences Press: Wuhan, China, 2022; pp. 73–194. (In Chinese with English Abstract)
38. Wang, J.X.; Zhang, K.X.; Jin, J.S.; Song, B.W.; Yu, Y.; Wang, L.J.; Wang, S.D.; Sun, S. Early Paleozoic ocean plate stratigraphy of the Beishan Orogenic Zone, NW China: Implications for regional tectonic evolution. *Acta Geol. Sin.* **2020**, *94*, 1042–1059. [[CrossRef](#)]
39. Huang, B.T.; Wang, G.Q.; Li, X.M.; Bu, T.; Dong, Z.C.; Zhu, T. Precambrian tectonic affinity of the Beishan Orogenic Belt: Constraints from Proterozoic metasedimentary rocks. *Precambrian Res.* **2022**, *376*, 106686–106698. [[CrossRef](#)]
40. Andersen, T. Correlation of common lead in U-Pb analyses that do not report ²⁰⁴Pb. *Chem. Geol.* **2002**, *192*, 59–79. [[CrossRef](#)]
41. Ludwig, K.R. *User's manual for Isoplot/Ex, Version 3.00, a Geochronological Toolkit for Microsoft Excel*; Berkeley Geochronology Center Special Publication: Berkeley, CA, USA, 2003; Volume 4, pp. 1–70.
42. Li, Y.G.; Wang, S.S.; Liu, M.W.; Meng, E.; Wei, X.Y.; Zhao, H.B.; Jin, M.Q. U-Pb study of baddeleyite by LA-ICP-MS: Technique and application. *Acta Geol. Sin.* **2015**, *89*, 2400–2418. (In Chinese with English Abstract)
43. Cai, Z.H.; Xu, Z.Q.; He, B.Z.; Wang, R.R. Age and tectonic evolution of ductile shear zones in the eastern Tianshan–Beishan orogenic belt. *Acta Petrol. Sin.* **2012**, *28*, 1875–1895. (In Chinese with English Abstract)
44. Liu, Y.S.; Hu, Z.C.; Zong, K.Q.; Gao, C.G.; Gao, S.; Xu, J.; Chen, H.H. Reappraisal and refinement of zircon U-Pb isotope and trace element analyses by LA-ICP-MS. *Chin. Sci. Bull.* **2010**, *55*, 1535–1546. [[CrossRef](#)]
45. Rubatto, D.; Gebauer, D. Use of cathodoluminescence for U-Pb zircon dating by ion microprobe: Some examples from the Western Alps. In *Cathodoluminescence in Geosciences*; Springer: Berlin/Heidelberg, Germany, 2000; pp. 373–400.
46. Möller, A.; O'Brien, P.J.; Kennedy, A.; Kröner, A. Linking growth episodes of zircon and metamorphic textures to zircon chemistry: An example from the ultrahigh-temperature granulites of Rogaland (SW Norway). *Geol. Soc. Spec. Publ.* **2003**, *220*, 65–81. [[CrossRef](#)]

47. Rollinson, H.R. *Using Geochemical Data: Evaluation, Presentation, Interpretation*; Longman Scientific & Technical Press: New York, NY, USA, 1993; pp. 1–352.
48. McDonough, W.F.; Sun, S.S. The composition of the Earth. *Chem. Geol.* **1995**, *120*, 223–253. [[CrossRef](#)]
49. Elthon, D.; Casey, J.F.; Komor, S. Mineral chemistry of ultramafic cumulates from the North Arm Mountain massif of the Bay of Islands ophiolite: Evidence for high-pressure crystal fractionation of oceanic basalts. *J. Geophys. Res.* **1982**, *87*, 8717–8734. [[CrossRef](#)]
50. Pearce, J.A.; Lippard, S.J.; Roberts, S. Characteristics and tectonic significance of supra-subduction zone ophiolites. *Geol. Soc. Spec. Publ.* **1984**, *16*, 77–94. [[CrossRef](#)]
51. Leblanc, M. Chromite growth, dissolution and deformation from a morphological view point: SEM investigations. *Miner. Deposita* **1980**, *15*, 201–210. [[CrossRef](#)]
52. Dick, H.J.B.; Bullen, T. Chromium spinel as a petrogenetic indicator in abyssal and alpine-type peridotites and spatially associated lavas. *Contrib. Mineral. Petrol.* **1984**, *86*, 54–76. [[CrossRef](#)]
53. Coleman, R.G. *Ophiolite Ancient Oceanic Lithosphere?* Springer: Berlin/Heidelberg, Germany, 1977; pp. 1–229.
54. Sun, S.S.; McDonough, W.F. Chemical and isotopic systematics of oceanic basalts: Implications for mantle composition and processes. *Geol. Soc. Spec. Publ.* **1989**, *42*, 313–345. [[CrossRef](#)]
55. Frey, F.A.; Green, D.H.; Roy, S.D. Integrated models of basalt petrogenesis: A study of quartz tholeiites to olivine melilitites from South Eastern Australia utilizing geochemical and experimental petrological data. *J. Petrol.* **1978**, *19*, 463–513. [[CrossRef](#)]
56. Nicolas, A.; Prinzhofer, A. Cumulative or residual origin for the transition zone in ophiolites: Structure evidence. *J. Petrol.* **1983**, *24*, 188–206. [[CrossRef](#)]
57. Hartmann, G.; Wedepohl, K.H. The composition of peridotite tectonics from the Ivrea complex, northern Italy, residues from melt extraction. *Geochim. Cosmochim. Acta* **1993**, *57*, 1761–1782. [[CrossRef](#)]
58. Yang, J.S.; Xiong, F.H.; Guo, G.L.; Liu, F.; Liang, F.H.; Chen, S.Y.; Li, Z.L.; Zhang, L.W. The Dongbo ultramafic massif: A mantle peridotite in the western part of the Yarlung Zangbo suture zone, Tibet, with excellent prospects for a major chromite deposit. *Acta Petrol. Sin.* **2011**, *27*, 3207–3222. (In Chinese with English Abstract)
59. Qiu, R.Z.; Deng, J.F.; Zhou, S.; Li, T.D.; Xiao, Q.H.; Guo, T.Y.; Cai, Z.Y.; Li, G.L.; Huang, G.C.; Meng, X.J. Ophiolite types in western Qinghai-Tibetan plateau—Evidences from petrology and geochemistry. *Earth Sci. Front.* **2005**, *12*, 277–291. (In Chinese with English Abstract)
60. Pearce, J.A. Ocean floor comes ashore. *Nature* **1991**, *354*, 110–111. [[CrossRef](#)]
61. Wilson, M. Review of igneous petrogenesis: A global tectonic approach. *Terra Nova* **1989**, *1*, 218–222. [[CrossRef](#)]
62. Condie, K.C. Geochemical changes in basalts and andsites across the Archaean–Proterozoic boundary: Identification and significance. *Lithos* **1989**, *23*, 1–18. [[CrossRef](#)]
63. Coleman, R.G.; Keith, T.E. A chemical study of serpentinization–Burro Mountain, California. *J. Petrol.* **1971**, *12*, 311–328. [[CrossRef](#)]
64. Dewey, J.F.; Bird, J. Origin and emplacement of the ophiolite suite: Appalachian ophiolites in Newfoundland. *J. Geophys. Res.* **1971**, *76*, 3179–3206. [[CrossRef](#)]
65. Moores, E.M.; Jackson, E.D. Ophiolites and oceanic crust. *Nature* **1974**, *250*, 136–139. [[CrossRef](#)]
66. Kidd, R.G.W. A model for the process of formation of the upper oceanic crust. *Geophys. J. R. Astron. Soc.* **1977**, *50*, 149–183. [[CrossRef](#)]
67. Dilek, Y.; Furnes, H. Ophiolite genesis and global tectonics: Geochemical and tectonic fingerprinting of ancient oceanic lithosphere. *Geol. Soc. Am. Bull.* **2011**, *123*, 387–411. [[CrossRef](#)]
68. Shi, R.D.; Yang, J.S.; Xu, Z.Q.; Qi, X.X. Recognition of MOR- and SSZ-type ophiolites in the Bangong Lake ophiolite mélange, western Tibet: Evidence from two kinds of mantle peridotites. *Acta Petrol. Mineral.* **2005**, *24*, 397–408. (In Chinese with English Abstract)
69. Arai, S. Characterization of spinel peridotites by olivine spinel compositional relationships: Review and interpretation. *Chem. Geol.* **1994**, *113*, 191–204. [[CrossRef](#)]
70. Meschede, M. A method of discriminating between different types of mid-ocean ridge basalts and continental tholeiites with the Nb–Zr–Y diagram. *Chem. Geol.* **1986**, *56*, 207–218. [[CrossRef](#)]
71. Mullen, E.D. MnO–TiO₂–P₂O₅: A minor element discriminant for basaltic rocks of oceanic environments and its implications for petrogenesis. *Earth Planet. Sci. Lett.* **1983**, *62*, 53–62. [[CrossRef](#)]
72. Wood, D.A. The application of a Th–Hf–Ta diagram to problems of tectonomagmatic classification and to establishing the nature of crustal contamination of basaltic lavas of the British Tertiary Volcanic Province. *Earth Planet. Sci. Lett.* **1980**, *50*, 11–30. [[CrossRef](#)]
73. Xiao, X.C.; Tang, Y.Q.; Feng, Y.M.; Zhu, B.Q.; Li, J.Y.; Zhao, M. *Crustal Structure and Geological Evolution in Xinjiang, China*; Geological Publishing House (China), Press: Beijing, China, 1992; pp. 1–169. (In Chinese)
74. Wang, B.Y. *Comprehensive Study on Geological Profile of Western Tianshan Mountain in China*; Science Press (China), Press: Beijing, China, 1994. (In Chinese)
75. Xia, L.Q.; Xia, Z.C.; Xu, X.Y.; Li, X.M.; Wang, L.S. Carboniferous Tianshan large igneous province and mantle plume. *Geol. Bull. China* **2004**, *23*, 903–910.
76. Xia, L.Q.; Xia, Z.C.; Xu, X.Y.; Li, X.M.; Ma, Z.P.; Wang, L.S. Relationships between Basic and Silicic Magmatism in Continental Rift Settings: A Petrogeochemical Study of the Carboniferous Post-collisional Rift Silicic Volcanics in Tianshan, NW China. *Acta Geol. Sin.* **2005**, *79*, 633–653.

77. Xia, L.Q.; Li, X.M.; Xu, X.Y.; Xia, Z.C.; Ma, Z.P.; Wang, L.S. Petrogenetic evolution of the Bayan Golophiolite-Geological record of an early Carboniferous “Red Sea Type” ocean basin in the Tianshan Mountains, Northwestern China. *Acta Geol. Sin.* **2005**, *79*, 174–192.
78. Wang, B.; Faure, M.; Shu, L.S.; Jong, K.D.; Charvet, J.; Cluzel, D.; Jahn, B.M.; Chen, Y.; Ruffet, G. Structural and Geochronological Study of High-Pressure Metamorphic Rocks in the Kekesu Section (Northwestern China): Implications for the Late Paleozoic Tectonics of the Southern Tianshan. *J. Geol.* **2010**, *118*, 59–77. [[CrossRef](#)]
79. Dong, Y.P.; Zhang, G.W.; Neubauer, F.; Liu, X.M.; Hauzenberger, C.; Zhou, D.W.; Li, W. Syn- and post-collisional granitoids in the Central Tianshan orogen. *Gondwana Res.* **2011**, *20*, 568–581.
80. Gao, J.; Klemm, R. Formation of HP-LT rocks and their tectonic implications in the western Tianshan Orogen, NW China: Geochemical and age constraints. *Lithos* **2003**, *66*, 1–22. [[CrossRef](#)]
81. Klemm, R.; Bocker, M.; Hacker, B.; Gao, J.; Gans, P.; Wemmer, K. New age constraints on the metamorphic evolution of the high-pressure/low-temperature belt in the Western Tianshan Mountains, NW China. *J. Geol.* **2005**, *113*, 157–168. [[CrossRef](#)]
82. Volkova, N.I.; Sklyarov, E.V. High-pressure complexes of Central Asian Fold Belt: Geologic setting, geochemistry, and geodynamic implications. *Russian Geol. Geophys.* **2007**, *48*, 83–90. [[CrossRef](#)]
83. Windley, B.F.; Allen, M.B.; Zhang, C.; Zhao, Z.Y.; Wang, G.R. Paleozoic accretion and Cenozoic reformation of the Chinese Tien Shan Range, central Asia. *Geology* **1990**, *18*, 128–131. [[CrossRef](#)]
84. Solomovich, L.I.; Trifonov, B.A. Postcollisional granites in the South Tien Shan Variscan Collisional Belt, Kyrgyzstan. *J. Asian Earth Sci.* **2002**, *21*, 7–21. [[CrossRef](#)]
85. Konopelko, D.; Biske, G.; Seltmann, R.; Eklund, O.; Belyatsky, B. Hercynian post-collisional A-type granites of the Kokshaal Range, Southern Tien Shan, Kyrgyzstan. *Lithos* **2007**, *97*, 140–160. [[CrossRef](#)]
86. Glorie, S.; Grave, J.D.; Zhimulev, F.; Buslov, M.; Izmer, A.; Vandoorne, W.; Ryabinin, A.; Elburg, M. Tectonic formation and Paleozoic evolution of the Gorny-Altai—Altai-Mongolia suture zones, revealed by zircon LA-ICP-MS U/Pb geochronology. In Proceedings of the 7th International symposium on Gondwana to Asia, Qingdao, China, 25–29 September 2010.
87. Xiao, W.J.; Han, C.M.; Yuan, C.; Sun, M.; Lin, S.F.; Chen, H.L.; Li, Z.L.; Li, J.L.; Sun, S. Middle Cambrian to Permian subduction-related accretionary orogenesis of Northern Xinjiang, NW China: Implications for the tectonic evolution of central Asia. *J. Asian Earth Sci.* **2008**, *32*, 2–4. [[CrossRef](#)]
88. Allen, M.B.; Windley, B.F.; Zang, C. Paleozoic collisional tectonics and magmatism of the Chinese Tianshan, central Asia. *Tectonophysics* **1992**, *220*, 89–115. [[CrossRef](#)]
89. Brookfield, M.E. Geological development and Phanerozoic crustal accretion in the western segment of the southern Tianshan (Kyrgyzstan, Uzbekistan and Tajikistan). *Tectonophysics* **2000**, *328*, 1–14. [[CrossRef](#)]
90. Zhang, J.X.; Meng, F.C.; Wan, Y.S. A cold Early Paleozoic subduction zone in the Northern Qilian Mountains, NW China: Petrological and U-Pb geochronological constraints. *J. Metamorph. Geol.* **2007**, *25*, 285–304. [[CrossRef](#)]
91. Li, X.M.; Yu, J.Y.; Wang, G.Q.; Wu, P.; Zhou, Z.Q. LA-ICP-MS zircon U-Pb dating of Devonian Sangejing Formation and Dundunshan Group in Hongliuyuan, Beishan area, Gansu Province. *Geol. Bull. China.* **2011**, *30*, 1501–1507. (In Chinese with English Abstract)
92. Tian, J.; Xin, H.T.; Teng, X.J.; Li, M.; Liao, Q.A.; Zhang, Y.; Ren, B.F. Petrogenesis and tectonic implications of the Late Silurian–Early Devonian bimodal intrusive rocks in the Central Beishan Orogenic Belt, NW China: Constraints by petrology, geochemistry and Hf isotope. *J. Earth Sci.* **2023**, *34*, 431–443. [[CrossRef](#)]
93. Shan, L.; Tao, W.; Ying, T.; Yanbin, W.; DaWei, H.; ZhiXia, O. Zircon U-Pb age, origin and its tectonic significances of Huitongshan Devonian K-feldspar granites from Beishan orogen, NW China. *Acta Petrol. Sin.* **2011**, *27*, 3055–3070. (In Chinese with English Abstract)

Disclaimer/Publisher’s Note: The statements, opinions and data contained in all publications are solely those of the individual author(s) and contributor(s) and not of MDPI and/or the editor(s). MDPI and/or the editor(s) disclaim responsibility for any injury to people or property resulting from any ideas, methods, instructions or products referred to in the content.